because of the increasing competition from reaction step (c). Therefore, MIF in (−a) or (b) cannot explain increasing $\Delta^{17}O$ with increasing pressure either. Only MIF caused by isotope-selective quenching of $HOCO^{\ddagger}$ in reaction step (c) would cause the $\Delta^{17}O$ values to increase with increasing pressure. However, in contrast to the observations, $\Delta^{17}O$ values should then vanish in the low-pressure limit, where $k = (k_a \times k_b)/(k_{-a} + k_b)$. Very effective quenching of $HOCO^{\ddagger}$ by H_2O and H_2O_2 could cause a discrepancy between the observed total pressure changes and the actual $HOCO^{\ddagger}$ quenching rate changes. However, even given the high quenching efficiency of H_2O [~10 times that of N_2 (23)], this mechanism seems insufficient to explain the low-pressure offset. Therefore, the established reaction mechanism for CO + OH indicates that MIF is produced in at least two elementary reaction steps, one of them being step (c), which induces the positive pressure dependence.

No theoretical explanation for the occurrence of MIF in CO + OH is available. It is questionable whether the recent theory that relates MIF to symmetry restrictions in the formation of certain complexes (24) can be directly applied to the reaction CO + OH. Nota bene, MIF in the important reaction O + $O_2 \rightarrow O_3$ also remains unexplained (25). Here, the rate coefficient for $^{16}O + ^{18}O^{18}O$ is 50% higher than the one for $^{18}O + ^{16}O^{16}O$.

MIF has been detected in each one of the important atmospheric trace gases O_3, CO_2, N_2O, and CO. As we now know the origin of MIF in CO, the effect promises to be useful in atmospheric chemistry, as nearly all sources introduce CO into the atmosphere with $\Delta^{17}O = 0$. Because of the sink reaction CO + OH, $\Delta^{17}O$ values increase, which makes MIF a direct measure for the aging of atmospheric CO by exposure to OH.

References and Notes

1. J. Bigeleisen, *Science* **147**, 463 (1965); _____ and M. Wolfsberg, *Adv. Chem. Phys.* **1**, 15 (1958); H. C. Urey, *J. Chem. Soc. London* **1947**, 562 (1947).
2. K. Mauersberger, *Geophys. Res. Lett.* **14**, 80 (1987).
3. M. H. Thiemens and J. E. Heidenreich, *Science* **219**, 1073 (1983).
4. R. K. Yoo and G. I. Gellene, *J. Chem. Phys.* **105**, 177 (1996); J. J. Colman et al., *Science* **273**, 774 (1996).
5. T. Röckmann et al., *J. Geophys. Res.* **103**, 1463 (1998).
6. J. C. Johnston and M. H. Thiemens, *ibid.* **102**, 25395 (1997); D. Krankowsky et al., *Geophys. Res. Lett.* **22**, 1713 (1995).
7. M. H. Thiemens, T. Jackson, K. Mauersberger, B. Schüler, J. Morton, *Geophys. Res. Lett.* **18**, 669 (1991); Y. L. Yung, A. Y. T. Lee, F. W. Irion, W. B. DeMore, J. Wen, *J. Geophys. Res.* **102**, 10857 (1997).
8. P. S. Hodder, C. A. M. Brenninkmeijer, M. H. Thiemens, *U.S. Geol. Circ. 1107* (1994).
9. A. K. Huff and M. H. Thiemens, *Eos (Fall Suppl.)* (1996).
10. S. S. Cliff and M. H. Thiemens, *Science* **278**, 1774 (1997).
11. The δ value is defined as $\delta^{18}O = (^{18}O/^{16}O)_{SA}/(^{18}O/^{16}O)_{ST} - 1$ (analogous for ^{17}O), which gives the isotopic ratio of a sample (SA) relative to a standard (ST), in this case Vienna Standard mean ocean water [R. Gonfiantini, *Nature* **271**, 534 (1978)].
12. C. A. M. Brenninkmeijer and T. Röckmann, *J. Geophys. Res.* **102**, 25477 (1997).
13. C. M. Stevens et al., *Int. J. Chem. Kinet.* **12**, 935 (1980).
14. C. A. M. Brenninkmeijer, *J. Geophys. Res.* **98**, 10,595 (1993).
15. _____ and T. Röckmann, *Rapid Commun. Mass Spectrom.* **12**, 479 (1998).
16. Greenblatt and Howard [G. D. Greenblatt and C. J. Howard, *J. Phys. Chem.* **93**, 1035 (1989)] reviewed the relevant literature and measured the exchange rate coefficient $k_{exch} < 10^{-15}$ cm³ molecule⁻¹ s⁻¹ for the excited $HOCO^{\ddagger}$ complex, which is 100 times slower than the reaction rate coefficient ($k_{reac} > 10^{-13}$ cm³ molecule⁻¹ s⁻¹) (19). Exchange in the stabilized HOCO radical does not affect the reactants, because HOCO cannot be reconverted to reactants at ambient temperatures (21, 22). Stevens et al. (13) measured the same ^{18}O fractionation factor for normal and highly enriched CO in a similar experiment to ours, thus excluding exchange for our conditions.
17. M. K. Dubey, R. Mohrschladt, N. M. Donahue, J. G. Anderson, *J. Phys. Chem.* **101**, 1494 (1997).
18. H. G. J. Smit, A. Volz, D. H. Ehhalt, H. Knappe, in *Stable Isotopes*, H.-L. Schmidt, H. Förstel, K. Heinzinger, Eds. (Elsevier, Amsterdam, 1982), pp. 147–152.
19. W. B. DeMore et al., *JPL Publ. 11* (1994).
20. I. W. M. Smith, *Chem. Phys. Lett.* **49**, 112 (1977).
21. M. Mozurkewitch, J. J. Lamb, S. W. Benson, *J. Phys. Chem.* **88**, 6435 (1984).
22. D. Fulle, H. F. Hamann, H. Hippler, J. Troe, *J. Chem. Phys.* **105**, 983 (1996).
23. G. Paraskevopoulos and R. S. Irwin, *ibid.* **80**, 259 (1983).
24. G. I. Gellene, *Science* **274**, 1344 (1996).
25. S. M. Anderson, D. Hülsebusch, K. Mauersberger, *J. Chem. Phys* **107**, 5385 (1997).
26. We thank the Atmospheric Environment Service of Canada, the Norwegian Polar Institute, and the Izaña Global Atmospheric Watch observatory for conducting sampling. Supported by the European Commission, DG XII.

A Correlation Between Ultra-Low Basal Velocities in the Mantle and Hot Spots

Q. Williams, J. Revenaugh, E. Garnero*

The statistical correlation between the locations of hot spots at the surface of Earth and the distribution of ultra-low-velocity zones at the base of the mantle has about a 1 percent chance of arising randomly. This correlation is more significant than that between hot spots and negative velocity anomalies in tomographic models of deep mantle compressional and shear velocity. This correlation is consistent with the notion that many hot spots originate in a low-velocity, probably partially molten layer at the core-mantle boundary and undergo little lateral deflection on ascent.

The underlying control on the geographic distribution of hot spots, linear chains of volcanic edifices whose source appears to be fixed relative to surface plate motions, is uncertain. Hot spots tend to be distributed near long-wavelength geoid highs (1) and mid-ocean ridges (2), each of which may in turn be associated with slow seismic velocities in the lower mantle (3, 4). The upwellings that give rise to hot spots are widely thought to originate as instabilities near the core-mantle boundary (CMB) (5, 6), as this region likely represents a major thermal boundary layer. Geophysical observations that support hot spots originating near the CMB have, however, been notably lacking (7), although possible geochemical evidence for such a provenance exists (8). Here we examine whether hot spots are correlated with the presence of recently discovered 5- to 40-km-thick features at the base of Earth's

mantle with compressional wave velocities depressed by as much as 10% from the overlying mantle (9–13). These ultra-low-velocity zones (ULVZs) are likely generated by the presence of partial melt at depth (10, 11); it is unclear whether this partial melt differs chemically from the overlying mantle through (for example) either iron enrichment or volatile enrichment (10).

Thus far, the Fresnel zones of seismic waves sample 44% of the CMB for the presence or absence of ULVZs and ULVZs have been observed to be present over 12% of the CMB (12, 13). The locations of the ULVZs are derived from diffracted compressional wave segments traveling along the mantle side of the CMB (9, 12, 14) and from reflected compressional waves that sample the upper boundary of this basal layer (11, 13) (Fig. 1). Where ULVZs have been detected, their thicknesses are >5 km; thinner zones may be present elsewhere, but an ~5-km thickness is required for detection. The thicknesses of the ULVZs vary by up to 40 km over distances of ~100 km (and possibly less) (9, 10); as such, the nonobservance of this feature does not preclude the presence of undetected patches

Department of Earth Sciences and Institute of Tectonics, University of California, Santa Cruz, CA 95064, USA.

*Present address: Seismological Laboratory, University of California, Berkeley, CA 94720, USA.

of isolated ULVZs with lateral dimensions on the order of tens of kilometers.

ULVZs are present in six distinct regions: beneath the northern and central Atlantic Ocean, beneath Africa, south of Australia, and beneath the southwestern and northern Pacific Ocean (Fig. 1). They do not appear to be present beneath the Americas or beneath southern and central Asia, each of which are regions with relatively few hot spots. For comparison, we used the modified hot spot catalog of Sleep (6, 15), comprising 47 hot spots and estimates of their buoyancy flux.

We calculated the significance of the correlation between the hot spot and ULVZ distribution of Fig. 1 using two separate but complementary statistical approaches. The first approach calculated the numbers (and fluxes) of hot spots lying above ULVZs compared with those expected on the basis of an areally uniform distribution of independent hot spots (16). This algorithm simply determines the probability that a given number (or flux) of hot spots lying above the ULVZs could arise through random processes (17). Our second approach calculated the probability that random rotations of the hot spot distribution can produce improved correlations with the structure of the lowermost mantle; this method is designed to remove biasing of our statistics by either spatial clustering (mutual dependence) of hot spots or by our spatial sampling of the ULVZs.

To determine how many hot spots lie above ULVZs, we indexed the presence or absence of this feature (Fig. 1) on a 1° by 1° grid. On the 60-km length scale of this sampling, a number of hot spots (such as Tahiti) lie above ULVZs. For hot spots near the boundary between ULVZs and zones that have not been seismically investigated (such as Hawaii and Pitcairn Island), we imposed that at least 10% of the area of underlying latitude-longitude grid cells within 2° of the hot spot must lie in the ULVZs (18). In regions where no ULVZ has been observed and known ULVZs are juxtaposed (such as the Tasman hot spot), the number of latitude-longitude grid cells within 2° of the hot spot within the ULVZs must exceed those in which no ULVZ has been detected by at least 10%.

To further assess the robustness of our correlations, we examined the correlation of hot spots and hot spot flux with tomographically derived compressional (P) (19) and shear (S) wave velocity (4) models of the lowermost ~300 km of the mantle. The spatial coverage of these P- and S-wave models is global, whereas our constraints on where the ULVZ is present or absent are not. We therefore sampled the tomographic models for the same 44% of the planet as was sampled for the ULVZ in Fig. 1 and conducted 10,000 Monte Carlo samplings of the global

models at the 44% level.

As shown in Fig. 2, 13 of 47 hot spots lie over the 12% of the CMB containing ULVZs, and 12 lie over the 32% of the CMB in which no ULVZs have been resolved (20) (the rest are over areas of the mantle that have not been sampled). For comparison with the P- and S-wave tomographic models, we selected the velocity contours that have the highest

correlation with the hot spot distribution. For similar areas, the ULVZs produced a better correlation with both hot spot distribution and flux than either of the best correlated contours of the tomographic models (Fig. 2; 11 of 47 hot spots lie beneath this contour in the S-wave model). The correlation of the shear-velocity tomographic model with the hot spot distribution decreases for progressively shal-
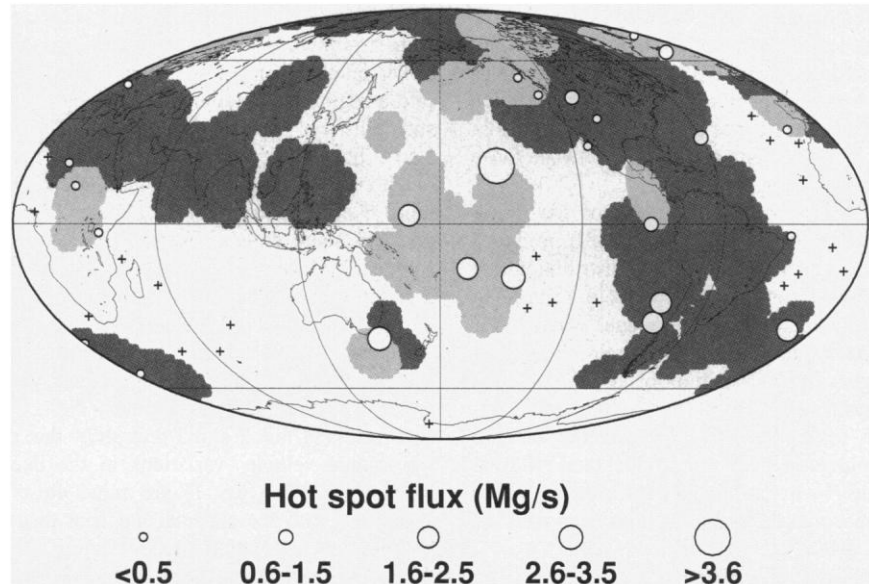

Hot spot flux (Mg/s)

∘	○	◯	◯	◯
<0.5	0.6-1.5	1.6-2.5	2.6-3.5	>3.6

Fig. 1. Known locations of ULVZs at the base of the mantle (12, 27). Light shading shows where this zone is ≥5 km thick, dark shading indicates where ULVZs are absent or less than ~5 km thick, and the absence of shading shows where no determinations have been made. Data under Eurasia and the Tasman Sea are from this study and use diffracted waves [for example, (9)]; all other data are from (9, 11–13, 28). Circles represent hot spots included in our analysis, with symbol size being proportional to flux (6), and crosses indicate hot spots above regions not yet seismically investigated for ULVZs.
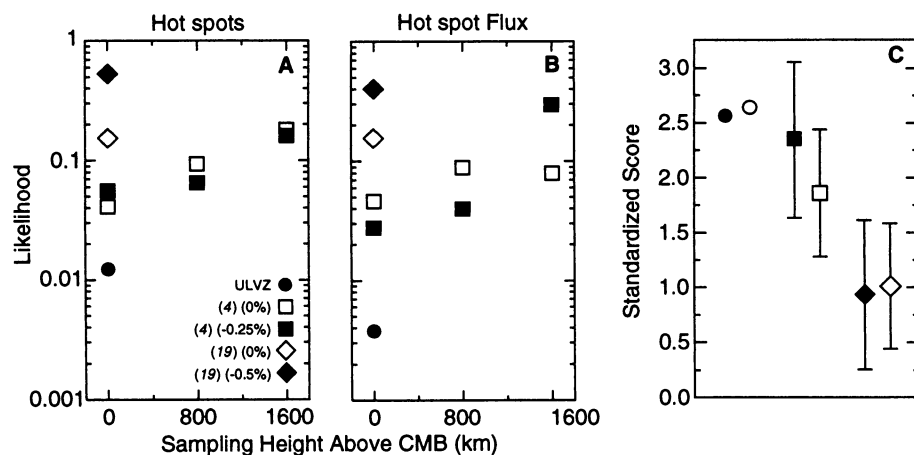

Fig. 2. Statistical likelihood and standardized scores of correlations of ULVZs and tomographic models with overlying numbers of hot spots and fluxes. (**A**) Probabilities that the number of hot spots above the ULVZs of Fig. 1 and above the best correlated velocity contours in the P- and S-wave tomographic models (4, 19) occurs randomly, for differing nominal sampling heights above the CMB. (**B**) Probabilities that the correlation between each model and the hot spot flux distribution represents a random occurrence. (**C**) Standardized scores (29) of correlations between the number of hot spots and the ULVZs, the −0.25% contour of the S-wave tomographic model (4), and the −0.5% P-wave velocity contour (19) (solid symbols) and between the hot spot flux, the ULVZs, and the two tomographic contours (open symbols); error bars reflect the SD of 10,000 random samplings of the tomographic models.

lower depths in the lower mantle.

The 0.0% velocity anomaly line, the boundary between slower than average and faster than average regions, provides the best tomographically derived prediction of hot spot location (Fig. 2). We attribute this correlation to the well-known avoidance between hot spots and cold downwelling regions of the mantle (1, 21, 22). The best match between the hot spot distribution and the tomographic models thus likely reflects a broad length-scale anticorrelation rather than a genetic correlation. In contrast, the correlation between the ultra-low-velocity (and thus probably hot) zones and hot spots is consistent with a genetic association between these features.

A random areal sampling of the tomographic models (at the 44% level) produced correlations with the hot spot distribution that are similar to those derived from a sampling of the same 44% of the planet with ULVZ characterization (Fig. 2C). Again, these samplings produced an inferior correlation with both hot spot flux and hot spot location relative to the ULVZ [<7% of the random samplings of the S-wave model (and <0.03% of the P-wave model) lie beneath more than 13 hot spots and are better correlated with hot spot flux].

To minimize possible spatial biases, we also randomly rotated the hot spot distribution 10,000 times. We used the 44% areal sampling of the CMB of Fig. 1 and determined how many random rotations produced

distributions of hot spot number or flux that improved on the match of the real hot spot distribution with the ULVZs (or with the tomographic models). Because there is some spatial clustering of hot spots, the marginal distribution of numbers and fluxes derived from random rotations exceeds that derived from a binomial distribution (Fig. 3, A and B); that is, anomalously large numbers of rotations produce an enhanced number (or flux) of hot spots relative to those expected from a random distribution. In this analysis, larger numbers of hot spots may be rotated into a region by random rotations, but most such clustered hot spots have smaller fluxes. Large hot spots tend to have fewer near neighbors, whereas smaller hot spots are more likely to cluster (6), with such clusters possibly being derived from the same basal source (23). Therefore, the combination of high numbers and high fluxes associated with the ULVZs again renders the correlation of this feature with the hot spot distribution more significant than the correlation with either of the tomographic models (Fig. 2C). The results in Fig. 2 and 3 thus show that of the known velocity variations in the deep mantle, ULVZs (Fig. 1) are most closely correlated with the surficial hot spot distribution. The correlation of this feature with flux-weighted hot spots has an ~1% probability of arising randomly, whereas the most closely correlated tomographic P- and S-wave velocity anomalies (4, 19) have about a 15 and 4% chance of being randomly pro-

duced, respectively.

The flux-weighted distribution of plumes is strongly peaked at spherical harmonic degrees 1 and 2 (15); this distribution is compatible with a 40-km-thick layer if the viscosity ratio between the overlying material and the boundary layer is greater than about 5×10^6. If the basal boundary layer of the mantle is 5 to 30% partially molten (10, 11), the viscosity of this layer could be depressed by substantially more than a factor of 5×10^6, in accord with the constraints of the power spectrum of hot spot distribution.

The general fixity of hot spots over time relative to plate motions indicates that the plumes tapping this anomalous basal layer, once established, have a relatively long lifespan. Our correlation implies either that hot spots require a moderately thick (on the order of 10 km) basal layer to persist or that the local fluid flow associated with the hot spot upwelling provides an efficient means for advecting heat from the surface of the core, resulting in a local upwarping of isotherms and the elevation of a partially molten horizon into the mantle. The correlation of the ULVZs with surface hot spot position further indicates that mantle convection may not notably deflect plumes (24). Our results also support the existence of feedback between plate tectonics and the CMB. Continental breakup has been proposed to be correlated with hot spots (25); if ULVZs control the hot spot distribution, then the lowermost mantle may control the location of divergent plate boundaries at Earth's surface (26). For comparison, subduction may modulate the distribution of hot spots (22); therefore, the location of the ULVZs could in turn be determined by past plate convergence.

Fig. 3. Probability that the correlation between ULVZs and hot spot number and flux arises randomly on the basis of random rotations of the hot spot distribution. (**A**) Logarithm of the probability that equal or greater numbers of hot spots lying above the ULVZs could arise by chance, with the solid line showing the calculated likelihood based on 10,000 random rotations of the hot spot distribution and the dashed line showing a binomial prediction. The vertical line shows the observed number of hot spots lying above the ULVZs. (**B**) Logarithm of probability of random occurrence of differing hot spot fluxes, in megagrams per second. (**C**) Contours of the cumulative probability (in logarithmic units) of producing differing combinations of hot spot flux and number, relative to that observed for the ULVZ (solid circle). (**D**) Probabilities that correlations between hot spot numbers, fluxes, and their combination could arise randomly for the ULVZs and for the same tomographic velocity contours as in Fig. 2.
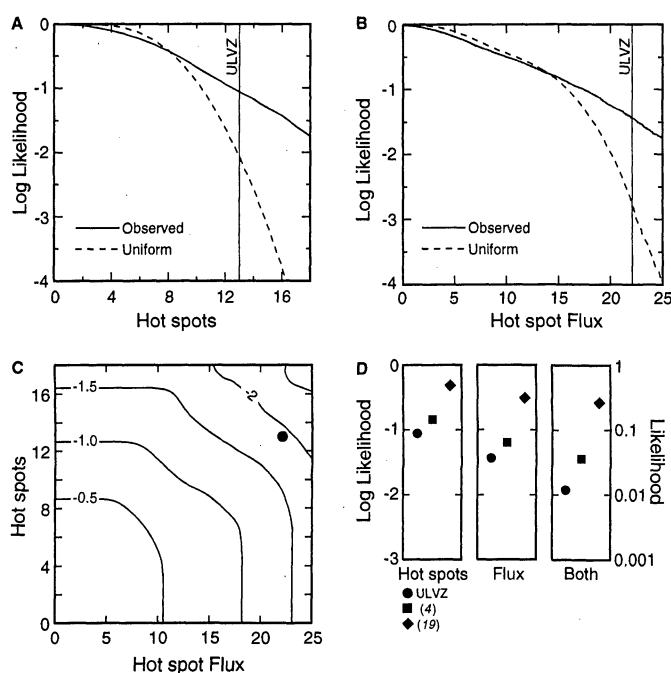
References and Notes

1. C. G. Chase, *Nature* **282**, 464 (1979); M. A. Richards, B. H. Hager, N. H. Sleep, *J. Geophys. Res.* **93**, 7690 (1988); S. T. Crough and D. M. Jurdy, *Earth Planet. Sci. Lett.* **48**, 15 (1980).
2. S. A. Weinstein and P. L. Olson, *Geophys. Res. Lett.* **16**, 433 (1989); D. M. Jurdy and M. Stefanick, *ibid.* **17**, 1965 (1990).
3. B. H. Hager, R. W. Clayton, M. A. Richards, R. P. Comer, A. M. Dziewonski, *Nature* **313**, 541 (1985).
4. W. Su, R. L. Woodward, A. M. Dziewonski, *J. Geophys. Res.* **99**, 6945 (1994).
5. D. E. Loper, *Phys. Earth Planet. Inter.* **34**, 57 (1984); P. Olson, G. Schubert, C. Anderson, *Nature* **327**, 409 (1987); G. F. Davies, *J. Geophys. Res.* **93**, 10467 (1988).
6. N. H. Sleep, *J. Geophys. Res.* **95**, 6715 (1990).
7. D. L. Anderson, T. Tanimoto, Y. Zhang, *Science* **256**, 1645 (1992); C. Moriceau, U. Christensen, L. Fleitout, *Earth Planet. Sci. Lett.* **103**, 395 (1991).
8. R. J. Walker, J. W. Morgan, M. F. Horan, *Science* **269**, 819 (1995).
9. E. Garnero and D. V. Helmberger, *Phys. Earth Planet. Inter.* **91**, 161 (1995); *Geophys. Res. Lett.* **23**, 977 (1996).
10. Q. Williams and E. J. Garnero, *Science* **273**, 1528 (1996); J. E. Vidale and M. A. H. Hedlin, *Nature* **391**, 682 (1998).
11. J. Revenaugh and R. Meyer, *Science* **277**, 670 (1997).
12. E. Garnero, J. Revenaugh, Q. Williams, T. Lay, L. Kellogg, in *The Core-Mantle Boundary Region*, M.

Gurnis, M. E. Wysession, E. Knittle, B. A. Buffett, Eds. (American Geophysical Union, Washington, DC, in press).

13. J. Mori and D. V. Helmberger, *J. Geophys. Res.* **100**, 20359 (1995).

14. In constructing Fig. 1, we incorporated only those ray paths for which anomalous diffracted *P*-wave segments of the seismic phase *SPdKS* could be resolved to lie on either the source or receiver side of the ray path, as derived from different paths containing overlapping diffracted segments (*9, 12*). The lateral extent of ULVZs was determined by standard Fresnel zone analysis (*19*) including all regions sampled within the first quarter period. Varying the assumed size of the Fresnel zone affected our statistical correlations, with smaller and larger zones producing somewhat worse correlations between hot spots and the ULVZs. Nevertheless, ULVZs are better correlated with hot spot flux than any contours within tomographic velocity models of the deep mantle (*4, 19*) for Fresnel zone dimensions between one-eighth and one-half wavelength.

15. N. M. Ribe and D. P. de Valpine, *Geophys. Res. Lett.* **21**, 1507 (1994).

16. T. W. Ray and D. L. Anderson, *J. Geophys. Res.* **99**, 9605 (1994).

17. S. T. Crough, *Tectonophysics* **61**, 321 (1979).

18. Our results are not particularly sensitive to our areal sampling size around hot spots; distances from 0.5° to 4° produce similar statistical correlations.

19. M. E. Wysession, *Nature* **382**, 244 (1996).

20. Those hot spots that lie above regions where ULVZs have not been observed could be (i) associated with highly localized (and as yet undetected) ULVZs, (ii) produced by lateral flow or deflection of plumes (*22*), or (iii) derived from a different depth or through a different process than ULVZ-associated hot spots.

21. C. G. Chase and D. R. Sprowl, *Earth Planet. Sci. Lett.* **62**, 314 (1983).

22. N. H. Sleep, *J. Geophys. Res.* **97**, 20007 (1992).

23. W. J. Morgan, *ibid.* **83**, 5355 (1978); N. H. Sleep, *ibid.* **101**, 28065 (1996).

24. P. Olson and I. S. Nam, *ibid.* **91**, 7181 (1986).

25. W. J. Morgan, *Tectonophysics* **94**, 123 (1983); B. C. Storey, *Nature* **377**, 301 (1995).

26. W. J. Morgan, *Geol. Soc. Am. Mem.* **132**, 7 (1972); R. E. Sheridan, *Tectonophysics* **143**, 59 (1987); M. A. Richards, R. A. Duncan, V. E. Courtillot, *Science* **246**, 103 (1989); I. H. Campbell and R. W. Griffiths, *Earth Planet. Sci. Lett.* **99**, 79 (1990).

27. T. Lay, Q. Williams, E. J. Garnero, *Nature* **392**, 461 (1998).

28. K. M. Fischer *et al.*, *Eos* **77**, F678 (1996).

29. Standardized score (*z*) is defined as $z = (O - E)/\sigma$, where *O* is the number of hot spots (or flux) inside a velocity contour for a randomly sampled 44% of the tomographic models, *E* denotes the number (or flux) predicted by a binomial distribution, and σ is the standard deviation of the binomial. Zero corresponds to uncorrelated data; $z \geq 1.0$ has an ~15% likelihood of arising randomly.

30. Supported by the NSF Geophysics and Presidential Faculty Fellow programs. We thank H. Nataf and the reviewers for comments on the manuscript.

20 March 1998; accepted 21 May 1998

Fast Recession of a West Antarctic Glacier

E. J. Rignot

Satellite radar interferometry observations of Pine Island Glacier, West Antarctica, reveal that the glacier hinge-line position retreated 1.2 ± 0.3 kilometers per year between 1992 and 1996, which in turn implies that the ice thinned by 3.5 ± 0.9 meters per year. The fast recession of Pine Island Glacier, predicted to be a possible trigger for the disintegration of the West Antarctic Ice Sheet, is attributed to enhanced basal melting of the glacier floating tongue by warm ocean waters.

Pine Island Glacier is a major ice stream of West Antarctica (*1–7*) that has been highlighted as being vulnerable to climate change and a possible trigger for the disintegration of the West Antarctic Ice Sheet (*6, 7*). The ice stream flows rapidly into Pine Island Bay, in the Amundsen Sea, unrestrained by a large ice shelf at its junction with the ocean, over a subglacial bed well below sea level, which deepens inland. This flow configuration is theoretically unstable (*8, 9*) because a retreat of its grounding line (where the glacier reaches the ocean and becomes afloat) would be self-perpetuating and irreversible, regardless of climate forcing.

Early estimates of the ice-stream mass budget suggested that it was thickening (*3, 4*). The result was called into question (*5*), but not enough reliable data existed on the ice flow and grounding line to allow a precise mass balance calculation. More recently, a hydrographic survey of Pine Island Bay revealed that the glacier experiences basal melt rates one order of magnitude larger than those recorded on large Antarctic ice shelves (*10, 11*). High

Jet Propulsion Laboratory, California Institute of Technology, MS 300-235, Pasadena, CA 91109–8099, USA. E-mail: eric@adelie.jpl.nasa.gov

basal melting is apparently fueled by an influx of relatively warm ocean waters from the southern Pacific Ocean (*10*). Such basal melting brings new considerations for the mass budget of the glacier floating section (*1*).

Here, I applied a quadruple difference interferometry technique (*12, 13*) on radar data gathered by the Earth Remote Sensing instruments (ERS-1 and -2) to detect the hinge-line position (or limit of tidal flexing) across Pine Island Glacier and its migration with time (*14*) (Fig. 1). Feature tracking based on the phase correlation method was used with the same data to yield detailed vector measurements of the glacier velocity on both grounded and floating ice (*15*). The glacier surface elevation was obtained from a new digital elevation model (DEM) of Antarctica (*16*).

Combining the glacier hinge-line position, velocity, and surface elevation, I calculated that the ice discharge is 76 ± 2 km³ of ice year⁻¹ at the hinge line (*17*). The estimated mass input from interior regions is 71 ± 7 km³ of ice year⁻¹ (*18*). These numbers suggest a mass deficit of 5 ± 7 km³ of ice year⁻¹ upstream of the hinge line (*19*).

The hinge-line positions retrieved in 1992, 1994, and 1996 (*20*) indicate a hinge-line retreat at a mean rate of 1.2 ± 0.3 km year⁻¹ (Fig. 1, B to F, and Fig. 2, A and B). Hinge-line retreat may result from an increase in sea-level height or a decrease in ice thickness (a decrease in the height of the seabed causes retreat too, but the effect is insubstantial over the time scale considered here) (*7–9*). Changes in sea level due to ocean tide yield an uncertainty in hinge-line position of less than 1.3 km per interferogram and 0.3 km year⁻¹ in mean retreat rate (*21*). I therefore attribute the 1992 to 1996 retreat to a decrease in ice thickness. The calculated rate of thinning is 3.5 ± 0.9 m of ice year⁻¹ at the hinge line.

Mass accumulation [+0.4 m year⁻¹ in (*1*)] and sublimation [−0.7 m year⁻¹ in (*22*)] at the glacier surface are too small to cause a major change in the glacier surface budget. A more likely explanation for the thinning is that the bottom melt rates experienced by the glacier have been too large to maintain the floating tongue in a state of mass balance (*23*).

Calculations of ice discharge seaward of the hinge line indicate that basal melting has exceeded 50 ± 10 m year⁻¹ in the first 20 km of the subice cavity, decreasing to an average of 24 ± 4 m year⁻¹ between the hinge line and the calving front (Fig. 2C). The large melt rates recorded near the hinge line imply that Pine Island Glacier is even more sensitive to ice-ocean interactions than was inferred from the 1994 survey of ice-front conditions (*10*).

Application of a two-dimensional thermohaline circulation model to the subice cavity reveals how sensitive basal melting is to changes in ocean conditions. An increase in seawater temperature from +1.5° to +2.0°C increases basal melting by 30% (*11*). A 3.5–m year⁻¹ thinning could therefore result from a one-tenth of a degree Celsius increase in seawater temperature, which is not unlikely for the deep water in